Giant Circular Dichroism at Visible Frequencies Enabled by Plasmonic Ramp-Shaped Nanostructures

Mohsen Rajaei, Jinwei Zeng, Mohammad Albooyeh, Mohammad Kamandi, Mina Hanifeh, Filippo Capolino, and H. Kumar Wickramasinghe*

Department of Electrical Engineering and Computer Science, University of California, Irvine, Irvine, California 92697, United States

Ⓢ Supporting Information

ABSTRACT: Plasmonic nanostructures with spatial symmetry breaking have a variety of applications, from enhancing the enantioselective detection of chiral molecules to creating photonics devices such as circular polarizers. Compared to their molecular counterparts, engineered nanostructures exhibit orders of magnitude larger circular dichroism (CD) at optical frequencies. Although 3D nanostructures such as nanohelices have been reported with high CD at mid-IR frequencies, such high CDs have not yet been achieved at visible frequencies with decent efficiencies. Here, we propose a planar array of plasmonic ramp-shaped nanostructures with an azimuthally gradient depth that exhibits a giant CD and dissymmetry factor at visible frequencies. The structure is fabricated on a gold-coated glass slide using focused ion beam (FIB) with gradient intensity to induce the required gradient depth, hence, breaking symmetry. Optical experimental characterization in the reflection spectrum shows a CD up to 64% and a dissymmetry factor up to 1.13 at 678 nm, in a good agreement with numerical simulations. We envision our proposed structure together with the suggested fabrication method to inspire the design of novel optical devices such as nanoscale circular polarizers and a host of chiral molecules to improve enantioselectivity in the pharmaceutical industry.

KEYWORDS: circular dichroism, chirality, chiral plasmonic nanostructures, plasmonics, symmetry breaking, anisotropy
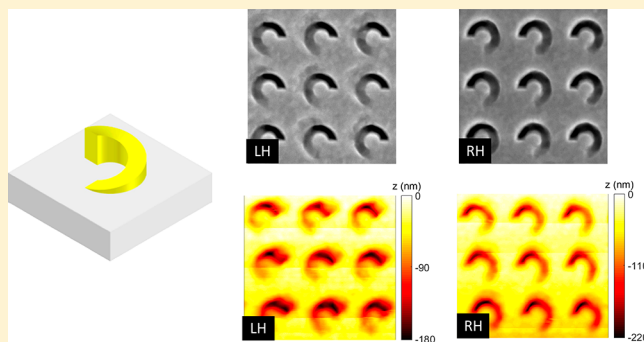
Plasmonic nanostructures with broken symmetry can show different electromagnetic response to left- and right-handed circularly polarized (LCP and RCP, respectively) light.[1−11] The different responses can be observed in both transmission[2,3] and reflection,[12] and the difference between the reflected (or transmitted) power under LCP and RCP illumination is often referred to as circular dichroism (CD),[2] which is a measure of the selectivity of the structure in interacting with the sense of handedness of the incident light. The concept of the CD used to describe artificially made nanostructures[2,6,13,14] is borrowed from the field of stereochemistry and is defined as the difference between the absorbance of LCP and RCP illumination by chiral molecules,[15−18] molecules that are not superimposable on their mirror-image by any rotation or translation.[19,20]

Although chiral molecules show different responses to LCP and RCP lights, their CD is very small due to their relatively weak interaction with light.[21−23] On the other hand, plasmonic nanostructures with broken symmetry can exhibit orders of magnitude higher CD.[1,8−11] This originates from the strong interaction of plasmonic nanostructures with light and creation of strong hot spots,[24−30] leading to many fascinating applications, including enantioselectivity enhancement,[14,31−36] engineered materials with negative index of refraction,[37] circular polarizers,[3−5] second-harmonic generation CD

(SHG-CD) microscopy,[38,39] light harvesting,[6] and chiral imaging.[7] Such applications are hard to achieve with naturally chiral materials due to their weak optical interaction. Therefore, extensive research studies have been recently performed on the design and fabrication of broken-symmetry nanostructures with highest possible achievable CDs.[8−11]

It is worth mentioning that CD measurements have been reported as the absolute[2] or normalized[13] LCP-RCP difference in different conventions. To avoid confusion, we consider the following definitions throughout this paper, that is, we assume the absolute difference is defined as CD = $L - R$, and the normalized difference is defined as $g = 2(L - R)/(L + R)$, which is called the g-factor or dissymmetry factor and has values between −2 to 2. Here, L and R are the transmittance or reflectance (the total transmitted or reflected power normalized to the incident power) when the excitation is LCP and RCP, respectively (i.e., the total measured or calculated reflected or transmitted power is the sum of the power in each polarization; in other words, no analyzers are used). Although the g-factor as a normalized quantity in some respects is a better descriptive measure, CD must be simultaneously monitored to show the absolute asymmetry

efficiency. Therefore, ideally, a broken symmetry plasmonic nanostructure should exhibit both a significant CD and a significant *g*-factor.

Several nanostructures have been introduced and reported to exhibit high CD. However, it is still a challenge to provide an effective high CD within the visible range.[2,6,13,33] For instance, the nanohelices fabricated by two-photon direct laser writing (DLW)[40] functions as broadband circular polarizers at mid-IR.[3−13] Smaller nanohelices or other broken symmetry nanostructures have been fabricated to be operative at the visible regime using other techniques, such as colloidal nanohole lithography for large-area fabrication,[2] glancing angle deposition (GLAD),[41,42] and focused ion and electron beam-induced deposition (FIBID and FEBID).[13] However, the maximum achieved CDs in the visible are not as high as those reported in the mid-IR. As another example, the plasmonic slanted nanoapertures in ref 7, fabricated with tilted focused ion beam (FIB) milling, show a high value of dissymmetry factor at visible frequencies (about 1.56 at 748 nm), but the CD is small (about 12%), which indicates a low energy efficiency.[7] In addition to the addressed top-down lithography methods, bottom-up techniques based on molecular self-assembly also offer a different route to fabricate broken symmetry structures with sub-10 nm resolution, but with even lower reported values of CDs in the visible range.[43,44] Therefore, it is essential to design plasmonic nanostructures that are not only convenient to fabricate but also offer a huge CD and dissymmetry factor at visible frequencies.

To that end, we propose a two-dimensional (2D) periodic array of three-dimensional (3D) plasmonic ramp-shaped nanostructures, which exhibits a giant CD in the reflection regime up to 64% as well as a huge dissymmetry factor up to 1.13 at the visible range. The proposed structure is fabricated using the FIB technique with a gradient milling approach to achieve the desired gradient depth (or height) and, hence, providing the required spatial symmetry breaking conditions to obtain a huge CD. Although the fabrication of both positive (removing the background and leaving the structure) and negative (removing the structure from the background) variants of the structure is possible, we focus on the negative structure since FIB technique results in a much better fabrication quality with more accurate nanogeometry compared to our desired structure. Therefore, since the proposed negative structure is mostly reflective, the CD is demonstrated in the reflection spectrum rather than the transmission one. We also support the experimental results with theoretical studies.

Before starting the discussion, we note that CD can originate from any kind of symmetry breaking of the structure, which can be either the structure's chirality or the structure's in-plane anisotropy (in the plane normal to the propagation direction).[45−50] The geometrical and material features of a structure are responsible for its electromagnetic properties, here described by chirality or anisotropy tensors (assuming the structure's response is well described by dipole approximations and ignoring higher-order multipoles), relating the electric and magnetic field components to the electric and magnetic dipole moments (see Supporting Information for a more detailed explanation). It is important to note that, although a structure may be chiral or in-plane anisotropic (by looking at the geometry), its electromagnetic response may or may not carry the signature of chirality or in-plane anisotropy since the scattered signature depends on the kind of chosen excitation.

In other words, one should select a proper excitation depending on what geometrical property is investigated.[51] Therefore, if a CD is obtained from a broken symmetry structure, referring to that structure as chiral or anisotropic may be confusing, and more analysis is required to determine the origin of the CD. A complete and thorough explanation about the origin of CD has been given in ref 51. Here, our structured surface is a reflective structure (transmission is almost zero), so we have only the reflection data, and not the transmission response, to analyze it and infer its properties. It can be shown that determining the origin of CD, that is, whether it is from chirality or from in-plane anisotropy, is not possible from only the amplitude of the reflection data.[51] Therefore, we cannot necessarily attribute the observed CD from our structure to chirality, although our structure is indeed geometrically chiral. That is why to describe our structure we refer to broken symmetry as a more general term. In summary, our study presents a new broken symmetry structure and fabrication technique for generating huge CD at the visible range, with such CD arising from chirality and anisotropy.

The organization of the paper is as follows. First, we introduce the ramp-shaped nanostructure, its geometry, and fabrication. Next we analyze the structure in both linear and circular polarization bases and present the CD measurement results. We also study the near-field distributions on the nanostructure, as illuminated by LCP and RCP light, to investigate the near-field origins of CD at different resonances of the nanostructure. We finally study the effect of the depth of the ramp-shaped nanostructure on CD and show that a relatively deep nanostructure is required to obtain such a giant CD. A conclusion and final remarks are presented at the end.

■ RESULTS AND DISCUSSION

Breaking the Symmetry: Introducing the Ramp-Shaped Nanostructure. Figure 1a shows a step by step fabrication procedure of a single unit cell of the proposed array of plasmonic nanostructures for both the positive and negative variants. A thin film of gold is deposited on a glass slide using an E-beam evaporator. A pattern is then made on the deposited gold using an FIB milling. The key fabrication idea is to upload a gray scale bitmap (BMP) file to the FIB machine. As shown in the upper row of Figure 1a, if the BMP file uploaded to the FIB machine is only black and white, the resulting output structure is then a uniform-height split ring, and consequently, such a structure demonstrates a zero CD in the experiment. However, uploading a gradient gray scale BMP file to the machine results in fabrication of a ramp-shaped structure with a gradient height (see the lower row of Figure 1 a), and therefore, is capable of providing a huge CD. We refer to these structures as *positive*. Now, uploading the negative BMP file of the first pattern, one achieves a reversed pattern, which we refer to as a *negative* structure. Therefore, in the positive structure, the height of the three-quarter split-ring gold nanostructure increases gradually, whereas in the negative one, the depth in the background gold increases gradually.

Figure 1b shows the schematic of one unit cell of the positive structure. The parameters of the structure, including the inner radius, width, height, and period of the array, were optimized to achieve a maximum possible CD at visible frequencies (see the caption of Figure 1 for values). As it can be seen in Figure 1a, the milling volume of the positive structure is about 10✕ more than that of the negative one, which causes a longer fabrication time with a lower quality for
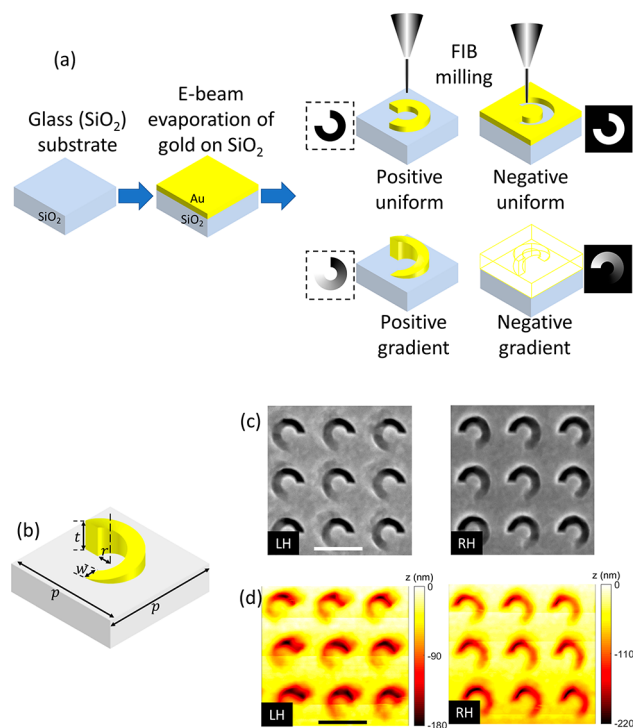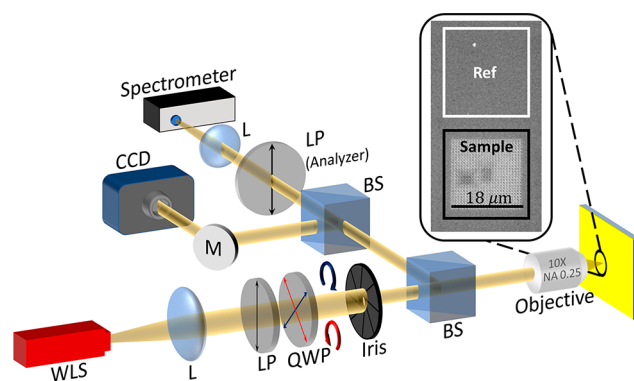
Figure 1. (a) Fabrication procedure of uniform/gradient and positive/negative variants of the ramp-shaped nanostructure. The gradient structure is realized using gradient milling with gradient BMP pattern. Also shown is the corresponding BMP pattern uploaded to the FIB machine for each case. (b) Schematic of one single unit-cell of the periodic array with $r = w = 100$ nm, $t = 200$ nm, and $p = 600$ nm, where p is the period of the array. (c) SEM and (d) AFM topography images of the left-handed (LH) and the right-handed (RH) structures. The darker pixels correspond to the deeper points. The scale bar is 600 nm.

Figure 2. Schematic of the experimental setup: WLS, white light source; L, lens; LP, linear polarizer; QWP, quarter-wave plate; BS, beam splitter; M, mirror; CCD, charge-coupled device. Second LP in front of the spectrometer acts as an analyzer. Also shown is the SEM image of an array of the ramp-shaped nanostructures. The adjacent area, which is gold-coated glass without any structure on it, is used as a reference for reflection measurements.

a positive structure compared to a negative one. Therefore, although based on the theoretical predictions and simulation results, both the negative and positive structures suggest huge CDs, we have focused on the fabrication and characterization of the negative structure, which is enough to prove the ability of the proposed structure as a device with a huge CD performance. Simulation results of the positive structure are presented in the Supporting Information. As a control experiment, we have further fabricated both the left- and right-handed (LH and RH) structures, which are expected to provide CDs with opposite signs.

Figure 1c,d shows the scanning electron microscopy (SEM) and atomic force microscopy (AFM) topography images of the fabricated structures. The gradient intensities prove that the gradient depth has successfully been achieved. The maximum depth for the LH and RH fabricated structures is 180 and 220 nm, respectively, which is close to the designed depth of 200 nm.

Optical Characterization Setup. The schematic of the measurement setup is shown in Figure 2. A collimated white light, generated by a tungsten-halogen lamp, is used as the source. The required circularly polarized (CP) light is generated via a linear polarizer and a quarter-wave plate (QWP) and is then focused on the sample by a 10× objective (NA = 0.25). Finally, the reflected light is read through a spectrometer and a charge-coupled device (CCD) camera. For analysis in linear polarization base, another linear polarizer is

used before the spectrometer as the analyzer. An iris is used to clip the beam, so that the beam is incident only on the center of the array and not on its edges.[52] Arrays of 18 μm by 18 μm (30 elements by 30 elements) were fabricated (see the SEM image in Figure 2), which are sufficiently larger than the focused beam spot on the array.

Analysis in Linear Polarization Base. We first analyze the structure in linearly polarized (LP) base. Since the QWPs do not have a perfect quarter retardance for all wavelengths, generated CP light may not be purely right or left; therefore, LP based measurements, in which no QWP is used, can be utilized to confirm fabrication quality. It is worth mentioning that LP-base responses could be used in determining the origin of the CD of some structures, whether it is chirality or in-plane anisotropy. However, in our case, the structure is reflective (the transmission is almost zero), so we have only the reflection data available, which is not enough to determine the origin of the CD.[51] Nevertheless, it is interesting to observe the results based on LP incidence here, which show the agreement between simulation and experiment and also verifies the fabrication and measurement setup. Figure 3 shows the reflection response of the LH structure in LP base. Co- and cross-polarized (co- and X-pol) coefficients of power reflection are shown for simulation and measurement. For example, xy means that the illuminating LP is oriented along the x-axis, and the received LP (analyzer) is oriented along the y-axis (Figure 2). The reference in all measurements is taken when the light is focused on an area without the patterned array, basically on a gold-coated glass substrate, which acts as a nearly perfect mirror (Figure 2). As shown in Figure 3, both X-pol coefficients are very small and do not exhibit any resonance in the experimental and simulation results. On the other hand, one strong absorption resonance is observed at 790 nm for xx (the dip in reflection), and two other small absorption dips are detected at 620 and 650 nm for both xx and yy cases in the experiment with lower amplitude for yy case. The full-wave simulation results, carried out with the finite element method (implemented by ANSYS Inc.), follow the same trend and confirm the experimental ones with some differences: the broad resonance for the xx case occurs at 824 nm rather than at 790 nm, which is observed from the experimental results; the lower-wavelength resonances are much sharper (for both
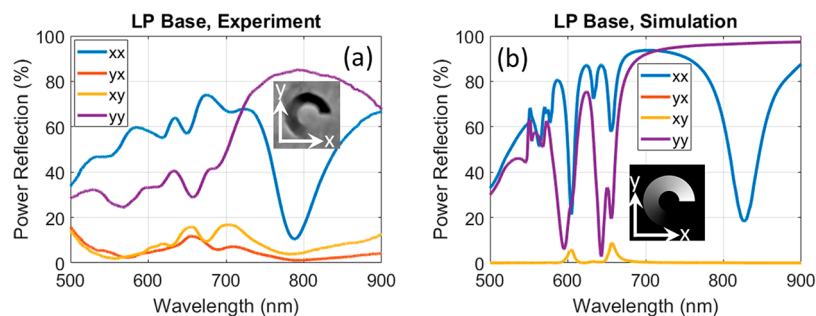
Figure 3. Characterization of the negative ramp-shaped structure in a linearly polarized base in (a) experiment and (b) simulation. The reflected power is normalized to the incident power, which is measured in the experiment as the power reflected from an unpatterned area, acting as a mirror. *ij* shows that the incident beam polarization is aligned along the *i*-axis, and the analyzer (reflected-field polarization) is along the *j*-axis, with *i* and *j* being either *x* or *y*. A broad resonance is observed at 790 nm (simulation) and 824 nm (measurement) for the *xx* case, and two sharper resonances occur at lower wavelengths around 620 and 650 nm for both *xx* and *yy* cases.
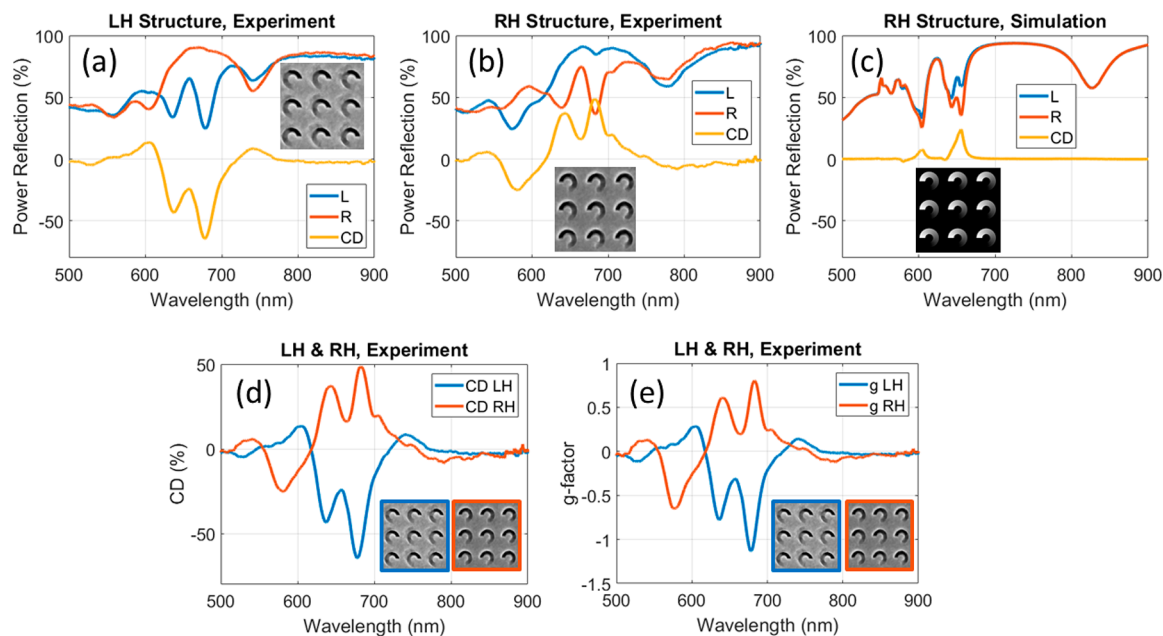

Figure 4. Characterization of the negative ramp-shaped structure when illuminated by electromagnetic wave with circular polarization and the CD measurement. (a, b) Reflectance coefficients for the LH and RH structures for incident beams with LCP (denoted by *L*) and RCP (denoted by *R*). Reflectance coefficients are defined as the total power (in both polarizations) divided by the incident LPC or RCP power. The difference between the reflectance coefficients is denoted by CD. A measured high CD of 64% and 49% is observed at 680 nm for the LH and the RH structures, respectively. (c) Simulation results of the reflected power for the RH structure. The maximum CD in the simulation is 24% at 655 nm. (d) Comparison between the measured CDs obtained from the LH and the RH structures. (e) Comparison between the measured *g*-factors of the LH and RH structures. A high *g*-factor of 1.13 and 0.8 is obtained for LH and RH structures, respectively. The small asymmetry in the measured results is due to fabrication imperfections and purity of the two senses of incident CP light handedness.

xx and *yy* cases) than those in the experiment and occur at around 595 and 643 nm. The slightly shifted and broadened resonances can be attributed to the imperfections in the fabrication (Figure 1c,d). However, what is important is the broken symmetry, which will result in a CD, demonstrated in the following section.

Analysis in Circular Polarization Base and Measurement of Circular Dichroism. Figure 4a,b shows the response of the LH and RH structures, each illuminated by LCP and RCP light, respectively. Here, we measure the total reflected power (the sum of the power in each reflected polarization); and "*L*" and "*R*" in the legend denote the reflectance coefficient (total reflected power normalized to the incident power) when the incident beam is an LCP or an RCP, respectively. Moreover, "CD" in the legend is defined as the difference between the reflectance coefficients in the two experiments

with LCP and RCP illuminations, that is, CD = *L* − *R*. Due to the symmetry inversion between the LH and RH structures, we expect from the theory that the *L* and *R* coefficients for the LH to be equal to the *R* and *L* coefficients for the RH structure. However, there is a small difference between the measured quantities (see Figure 4a,b), which is attributed to the imperfections of the QWPs, which do not have a perfect quarter retardance for all wavelengths, and hence, their outputs do not provide purely LCP or RCP lights to be used as the excitation beams. Nevertheless, the results are quite promising and clearly show the trends. Indeed, the symmetries in reflectance coefficients discussed above (*L*/*R* and *R*/*L* for LH and RH structures, respectively) are regarded as a control experiment, which proves the property of our experimental setup together with the optical activity (asymmetric reflection)
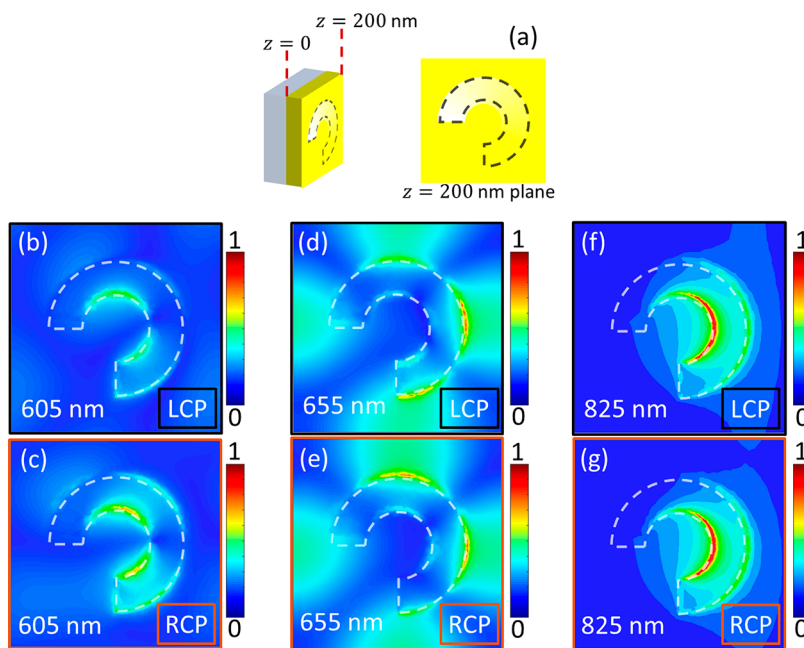
Figure 5. Distribution of the normalized electric field on the top surface of the RH structure illuminated with LCP and the RCP light, at three distinct wavelengths corresponding to the three major resonances. (a) Illustration of the $z = 200$ nm plane, the top face of the RH structure, at which the electric field is shown. (b−g) Field distribution at three major resonances (refer to Figure 4c) at 605, 655, and 825 nm for both LCP and RCP illuminations. While the distributions are different at 605 and 655 nm for the LCP and the RCP incidences, they are almost the same at 825 nm, which agrees with the observed nonzero CD at 605 and 655 nm and zero CD at 825 nm in Figure 4c. All the fields are normalized to $E_0 = 1.76 \times 10^9$, the maximum observed value of the total electric field for the LCP case at 825 nm.

of the proposed structure to illumination waves with opposite handedness (i.e., LCP and RCP) at around 640 and 680 nm.

From Figure 4a,b, we observe three distinct resonances (reflection dips) at around 640, 680, and 740 nm. While the behavior of the reflectance spectra (red and blue curves in Figure 4a,b) for the first two resonances at 640 and 680 nm is asymmetric for the illuminations with opposite senses of handedness, that of the third resonance at 740 nm is symmetric. Therefore, we observe considerable CDs (yellow curves in Figure 4a,b) at 640 and 680 nm, whereas the CD is almost zero at 740 nm. Note that the maximum CD is obtained at 680 nm and is 64% and 49% for the LH and the RH structures, respectively. The experimental results are in agreement with the full-wave simulation results in Figure 4c. Note that we have only shown the simulation results for the RH structure since the simulation results for the LH structure are perfectly matched to the dual of the RH structure. Comparison of Figure 4a,b with Figure 3c demonstrates that the simulation results are generally confirming the experimental results with the following differences.

First, the two lower resonance frequencies are red-shifted whereas the upper one is blue-shifted in simulations compared to the experiments. Basically, the resonance shift is due to two reasons: (a) the dimensions of the fabricated design do not match those of the simulations and (b) the materials (gold and glass) are not exactly the same in the fabrication and simulation designs. However, the different shift behaviors for the different resonance frequencies are explained as follows: the first lower resonances are attributed to the resonant behavior of the array inclusions, that is, the proposed ramp-shaped split rings, whereas the upper resonance is associated with the array period. This is exactly the reason why there is no difference between the reflectance spectra for the two LCP and RCP illuminations at the upper resonance in contrast to the

two lower resonances. Therefore, it is normal to observe different shift behaviors for these two sets of resonances, that is, the array inclusion and period resonances. Indeed, the mismatch between the parameters of the fabricated and simulated designs, which are related to the inclusion resonances, caused a blue-shift in resonances, whereas those mismatch parameters associated with the array period result in a red-shift.

Second, the resonance bandwidths are narrower in the simulation results as compared to the experimental results. The reason is attributed to a mismatch between the material losses in the fabricated and simulated designs.

Finally, the observed values of CD are smaller in the simulations compared to the experiments. Such a difference is attributed to the imperfections in the fabrication (Figure 1c,d). Specifically, the AFM topography images (Figure 1d) show that the width of the ramp-shaped structure is not uniform, the transition from the deepest (darkest) to the highest (brightest) points is not very smooth, and the edges are not sharp. Given the limitations of FIB milling (especially gradient milling in this case) such imperfections are inevitable. However, such imperfections are not harmful, and they are even in favor of the observation of larger CDs in experiments compared to the simulations. This is because an additional anisotropy is introduced to the ramp-shaped structure due to the fabrication imperfections (see Figure 1d); that is, the width of the ramp is not uniform, and it is wider at deeper points while narrower at the higher points. Such an enhanced anisotropy helps to increase the value of CD by contributing to the cross components reflected power. Other sources of disagreement between the values of the observed CD are perhaps associated with the degradation of the CPLs induced by the optics used in the setup (mirrors and beam splitters), as discussed in the Supporting Information.

The other important factor commonly used in the literature for characterization of the chiral nanostructures, as mentioned earlier, is a normalized difference or *g*-factor, defined as $g = 2(L − R)/(L + R)$, shown in Figure 4e. The maximum measured *g*-factor obtained at ∼680 nm is 1.13 and 0.8 for LH and RH structures, respectively. The small asymmetry is due to fabrication imperfections and purity of the incident CP lights.

Near-Field Distributions on the Ramp-Shaped Nanostructure. Next, to further elaborate the distinctive behavior of the structure with respect to two illuminations with different sense of handedness, we examine the normalized near-field distribution of the RH structure when illuminated with an LCP and an RCP at its three major resonances, namely, at 605, 655, and 825 nm, shown in Figure 4c. The CD, as a far-field response, originates from the asymmetric near-field distributions of the structure in response to LCP and RCP illuminations; therefore, we theoretically expect to observe asymmetric near-field behaviors at the wavelengths with nonzero CDs. Figure 5 shows the distribution of the simulated electric field on a cut-plane on the gold surface (crossing the aperture at $z = 200$ nm of the ramp-shaped structure on the illumination side) at the three resonances in response to LCP and RCP incidences. All fields are normalized to the maximum value of the total electric field in Figure 5f, which is the highest value among all the cases in Figure 5b−g. The kind of response of the structure at the two lower resonances (i.e., 605 and 655 nm) is distinct from that at the resonance at 825 nm. At 825 nm, although the structure is at resonance, and the electric field demonstrates a hot spot at the inner edge of the ramp, the field distribution for LCP and RCP illumination cases are almost the same. This is in complete agreement with the zero CD observed at 825 nm in Figure 4c. On the other hand, as explained before, at 605 and 655 nm, the near-fields of the structure show distinct behaviors for LCP and RCP illuminations, that is, although the positions of the hot spots are fixed, the values of the fields are obviously different for the two kinds of CP illuminations in each hot spot, correlating to the observed CD at these wavelengths (see Figure 4c).

Effect of the Depth of the Ramp-Shaped Nanostructure on the Circular Dichroism. Finally, we study the effect of the depth of the ramp-shaped gold nanostructure and correlate it to the obtained CD. Simulations in Figure 6 shows the effect of the depth of the ramp-shaped structure on the maximum achievable CD. Also shown is the wavelength at which this maximum occurs. As it can be seen, a shallow structure, having the depth of 100 nm, that is, equal to half of the designed depth (200 nm), shows almost no CD and acts as an almost symmetric planar structure. Note that, in the simulations, the structure is located on a glass substrate, and as it is observed, even the *z*-asymmetry of the structure does not generate significant CD for this thin case. Therefore, it is important to have a relatively deep structure to achieve a high CD at visible wavelengths. Note that similar crescent positive structures with low height have been proposed and reported to exhibit much lower CDs compared to our proposed structure.[2,6] The results in Figure 6 justify our choice for a depth of 200 nm for the gold ramp structure, considering also fabrication limitations since deeper structures prevent us from making smaller features with FIB.

CONCLUSIONS

We presented a 2D planar array of 3-D plasmonic azimuthally graded-depth ramp-shaped nanostructures that show a giant
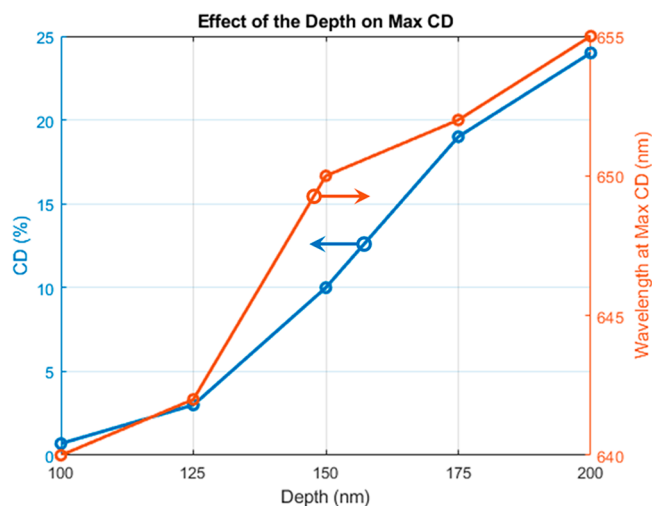
Figure 6. Effect of the ramp's depth (i.e., the thickness of the gold layer) of the ramp-shaped structure on the maximum achievable CD, and the change of the corresponding resonant wavelength at which maximum CD is observed. This graph shows the importance of having a significant ramp depth as halving the depth almost eliminates the maximum CD. Thickness is important to observe broken symmetry and, hence, CD.

CD at visible frequencies. Experimental and numerical results show three major resonance wavelengths in the reflection spectrum, two of which show asymmetric reflections when excited with LCP and RCP, resulting in a giant CD, whereas one of the resonances exhibits almost no CD. The structure shows a very high CD up to 64% and a *g*-factor up to 1.13 at 678 nm. Based on the reflection response of the structure in the LP base, we also concluded that the origin of the giant CD may not be due to its chirality, although the structure exhibits broken mirror symmetry and is indeed chiral. The ramp-shaped nanostructure is simply realized with a gradient milling using focused ion beam. The giant CD obtained by this structure at visible wavelengths as well as its simple fabrication overcomes the challenges of design and realization of complicated 3D nanohelical plasmonic structures. We believe this study is providing a physical insight into the response of photonic structures made of chiral/anisotropic unit cells, and is useful for the design of circular polarizers as well as for biosensors that are enantioselective of chiral molecules. It is important to note that enantioselectivity of chiral molecules using a chiral plasmonic nanostructure as the host can be tricky, as the CD generated by the host itself can be much stronger than that of the molecules. Therefore, a comparison between the CD with and without chiral molecules should be performed, and the change in the CD when the molecules are added should be recorded. A symmetric structure, as a host, that does not generate any CD, but enhances the chiral fields (i.e., helicity), would be a better option, as any CD obtained from the host−molecule system would be attributed to the molecules. These details have been thoroughly discussed in refs 35, 36, and 53.

METHODS

Fabrication. Gold deposition on a glass slide was done using electron-beam evaporation with an Angstrom evaporator. The FIB millings were done at 30 kV and 1.5 pA with a FEI Quanta 3D SEM/FIB machine. The fabrication time for a single unit cell was about 20 s.

Optical Characterization. The optical elements used in the characterization setup were as follows: White light source: Tungsten-halogen light source, 360−2600 nm, Thorlabs (SLS201L); White light source collimated: Collimation package, Thorlabs (SLS201C); Linear polarizer: Thorlabs (LPVIS050-MP2); Quarter-wave plate: Achromatic QWP, 400−800 nm, Thorlabs (AQWP05M-600); Objective lens: 10×, 0.25 NA, Newport (M-10X); CCD camera: AMScope 10MP digital camera; Spectrometer: Ocean Optics Flame.

Simulation. Numerical simulations are conducted using commercially available software tools based on the finite-element method (ANSYS Electronics Desktop 2017). Periodic boundary conditions are used in the simulations. CD spectra are calculated by extracting the left-handed and right-handed reflected fields at the ports, approximately two wavelengths away from the structure. The gold permittivity used in the simulations is taken from the experimental data by Johnson and Christy.[54] The glass permittivity is taken from the experimental data by Malitson.[55]

■ ASSOCIATED CONTENT

Ⓢ Supporting Information

The Supporting Information is available free of charge on the ACS Publications website at DOI: 10.1021/acsphotonics.8b01584.

On the definition of chirality and anisotropy based on geometry and electromagnetic response, analysis of positive structure, and degradation of the CPL by the optics (PDF).

■ AUTHOR INFORMATION

Corresponding Author

*E-mail: hkwick@uci.edu.

ORCID ⊙

Mohsen Rajaei: 0000-0001-8918-5539

Jinwei Zeng: 0000-0001-5795-2406

Mohammad Kamandi: 0000-0002-9135-8686

Author Contributions

M.R. and J.Z. did the fabrication and optical characterization. M.A., M.R., M.K., and M.H. did the simulations. H.K.W. and F.C. supervised the whole project. The manuscript was written with contributions of all authors. All authors have given approval to the final version of the manuscript.

Notes

The authors declare no competing financial interest.

■ REFERENCES

(1) Smith, K. W.; Link, S.; Chang, W.-S. Optical Characterization of Chiral Plasmonic Nanostructures. *J. Photochem. Photobiol., C* **2017**, *32* (Supplement C), 40−57.

(2) Frank, B.; Yin, X.; Schäferling, M.; Zhao, J.; Hein, S. M.; Braun, P. V.; Giessen, H. Large-Area 3D Chiral Plasmonic Structures. *ACS Nano* **2013**, *7* (7), 6321−6329.

(3) Gansel, J. K.; Thiel, M.; Rill, M. S.; Decker, M.; Bade, K.; Saile, V.; von Freymann, G.; Linden, S.; Wegener, M. Gold Helix Photonic Metamaterial as Broadband Circular Polarizer. *Science* **2009**, *325* (5947), 1513−1515.

(4) Gansel, J. K.; Latzel, M.; Frölich, A.; Kaschke, J.; Thiel, M.; Wegener, M. Tapered Gold-Helix Metamaterials as Improved Circular Polarizers. *Appl. Phys. Lett.* **2012**, *100* (10), 101109.

(5) Zhao, Y.; Belkin, M. A.; Alù, A. Twisted Optical Metamaterials for Planarized Ultrathin Broadband Circular Polarizers. *Nat. Commun.* **2012**, *3*, 870.

(6) Fang, Y.; Verre, R.; Shao, L.; Nordlander, P.; Kall, M. Hot Electron Generation and Cathodoluminescence Nanoscopy of Chiral Split Ring Resonators. *Nano Lett.* **2016**, *16* (8), 5183−5190.

(7) Chen, Y.; Gao, J.; Yang, X. Chiral Metamaterials of Plasmonic Slanted Nanoapertures with Symmetry Breaking. *Nano Lett.* **2018**, *18*, 520.

(8) Hentschel, M.; Schäferling, M.; Duan, X.; Giessen, H.; Liu, N. Chiral Plasmonics. *Sci. Adv.* **2017**, *3* (5), No. e1602735.

(9) Valev, V. K.; Baumberg, J. J.; Sibilia, C.; Verbiest, T. Chirality and Chiroptical Effects in Plasmonic Nanostructures: Fundamentals, Recent Progress, and Outlook. *Adv. Mater.* **2013**, *25* (18), 2517−2534.

(10) Govorov, A. O.; Gun'ko, Y. K.; Slocik, J. M.; Gérard, V. A.; Fan, Z.; Naik, R. R. Chiral Nanoparticle Assemblies: Circular Dichroism, Plasmonic Interactions, and Exciton Effects. *J. Mater. Chem.* **2011**, *21* (42), 16806−16818.

(11) Kumar, J.; Thomas, K. G.; Liz-Marzán, L. M. Nanoscale Chirality in Metal and Semiconductor Nanoparticles. *Chem. Commun.* **2016**, *52* (85), 12555−12569.

(12) Mousavi, S. H. S.; Panikkanvalappil, S. R.; El-Sayed, M. A.; Eftekhar, A. A.; Adibi, A. Large Enhancement of Circular Dichroism Using an Embossed Chiral Metamaterial. *arXiv:1604.05244 [physics.optics]* **2016**, na.

(13) Esposito, M.; Tasco, V.; Cuscunà, M.; Todisco, F.; Benedetti, A.; Tarantini, I.; Giorgi, M. D.; Sanvitto, D.; Passaseo, A. Nanoscale 3D Chiral Plasmonic Helices with Circular Dichroism at Visible Frequencies. *ACS Photonics* **2015**, *2* (1), 105−114.

(14) Schäferling, M.; Dregely, D.; Hentschel, M.; Giessen, H. Tailoring Enhanced Optical Chirality: Design Principles for Chiral Plasmonic Nanostructures. *Phys. Rev. X* **2012**, *2* (3), 031010.

(15) Fasman, G. D. *Circular Dichroism and the Conformational Analysis of Biomolecules*; Springer Science & Business Media, 2013.

(16) Amabilino, D. B. *Chirality at the Nanoscale: Nanoparticles, Surfaces, Materials and More*; John Wiley & Sons, 2009.

(17) Behr, J.-P. *The Lock-and-Key Principle: The State of the Art−100 Years On*; John Wiley & Sons, 2008.

(18) Eyring, H.; Liu, H.-C.; Caldwell, D. Optical Rotatory Dispersion and Circular Dichroism. *Chem. Rev.* **1968**, *68* (5), 525−540.

(19) Berova, N.; Nakanishi, K.; Woody, R. *Circular Dichroism: Principles and Applications*; John Wiley & Sons, 2000.

(20) Kelvin, W. T., Baron; Thomson, W. *Baltimore Lectures on Molecular Dynamics and the Wave Theory of Light*; Cambridge University Press, 2010.

(21) Zeng, J.; Albooyeh, M.; Darvishzadeh-Varcheie, M.; Kamandi, M.; Veysi, M.; Hanifeh, M.; Rajaei, M.; Albee, B.; Potma, E. O.; Wickramasinghe, H. K.; et al. Unveiling Magnetic and Chiral Nanoscale Properties Using Structured Light and Nanoantennas. In *2017 11th International Congress on Engineered Materials Platforms for Novel Wave Phenomena (Metamaterials)*; IEEE, 2017; pp 391−393; DOI: 10.1109/MetaMaterials.2017.8107824.

(22) Kamandi, M.; Albooyeh, M.; Guclu, C.; Veysi, M.; Zeng, J.; Wickramasinghe, K.; Capolino, F. Enantiospecific Detection of Chiral Nanosamples Using Photoinduced Force. *Phys. Rev. Appl.* **2017**, *8* (6), 064010.

(23) Kamandi, M.; Albooyeh, M.; Veysi, M.; Rajaei, M.; Zeng, J.; Wickramasinghe, H. K.; Capolino, F. Unscrambling Structured Chirality with Structured Light at the Nanoscale Using Photoinduced Force. *ACS Photonics* **2018**, *5* (11), 4360−4370.

(24) Simeone, D.; Esposito, M.; Scuderi, M.; Calafiore, G.; Palermo, G.; De Luca, A.; Todisco, F.; Sanvitto, D.; Nicotra, G.; Cabrini, S.

Tailoring Electromagnetic Hot Spots toward Visible Frequencies in Ultra-Narrow Gap Al/Al2O3 Bowtie Nanoantennas. *ACS Photonics* **2018**, *5*, 3399.

(25) Halas, N. J.; Lal, S.; Chang, W.-S.; Link, S.; Nordlander, P. Plasmons in Strongly Coupled Metallic Nanostructures. *Chem. Rev.* **2011**, *111* (6), 3913−3961.

(26) Brongersma, M. L.; Shalaev, V. M. The Case for Plasmonics. *Science* **2010**, *328* (5977), 440−441.

(27) Thrift, W. J.; Nguyen, C. Q.; Darvishzadeh-Varcheie, M.; Zare, S.; Sharac, N.; Sanderson, R. N.; Dupper, T. J.; Hochbaum, A. I.; Capolino, F.; Abdolhosseini Qomi, M. J.; et al. Driving Chemical Reactions in Plasmonic Nanogaps with Electrohydrodynamic Flow. *ACS Nano* **2017**, *11* (11), 11317−11329.

(28) Darvishzadeh-Varcheie, M.; Guclu, C.; Ragan, R.; Boyraz, O.; Capolino, F. Electric Field Enhancement with Plasmonic Colloidal Nanoantennas Excited by a Silicon Nitride Waveguide. *Opt. Express* **2016**, *24* (25), 28337−28352.

(29) Zhang, Y.; Demesy, G.; Haggui, M.; Gérard, D.; Béal, J.; Dodson, S.; Xiong, Q.; Plain, J.; Bonod, N.; Bachelot, R. Nanoscale Switching of Near-Infrared Hot Spots in Plasmonic Oligomers Probed by Two-Photon Absorption in Photopolymers. *ACS Photonics* **2018**, *5* (3), 918−928.

(30) Rajaei, M.; Almajhadi, M. A.; Zeng, J.; Wickramasinghe, H. K. Near-Field Nanoprobing Using Si Tip-Au Nanoparticle Photoinduced Force Microscopy with 120:1 Signal-to-Noise Ratio, Sub-6-Nm Resolution. *Opt. Express* **2018**, *26* (20), 26365−26376.

(31) Hendry, E.; Carpy, T.; Johnston, J.; Popland, M.; Mikhaylovskiy, R. V.; Lapthorn, A. J.; Kelly, S. M.; Barron, L. D.; Gadegaard, N.; Kadodwala, M. Ultrasensitive Detection and Characterization of Biomolecules Using Superchiral Fields. *Nat. Nanotechnol.* **2010**, *5* (11), 783−787.

(32) Ma, W.; Kuang, H.; Xu, L.; Ding, L.; Xu, C.; Wang, L.; Kotov, N. A. Attomolar DNA Detection with Chiral Nanorod Assemblies. *Nat. Commun.* **2013**, *4*, na.

(33) Zhao, Y.; Askarpour, A. N.; Sun, L.; Shi, J.; Li, X.; Alù, A. Chirality Detection of Enantiomers Using Twisted Optical Metamaterials. *Nat. Commun.* **2017**, *8*, 14180.

(34) Vázquez-Guardado, A.; Chanda, D. Superchiral Light Generation on Degenerate Achiral Surfaces. *Phys. Rev. Lett.* **2018**, *120* (13), 137601.

(35) Hanifeh, M.; Albooyeh, M.; Capolino, F. Helicity Maximization of Structured Light to Empower Nanoscale Chiral Matter Interaction. *ArXiv 180904119 Phys.* **2018**, na.

(36) Hanifeh, M.; Albooyeh, M.; Capolino, F. Optimally Chiral Electromagnetic Fields: Helicity Density and Interaction of Structured Light with Nanoscale Matter. *ArXiv 180904117 Phys.* **2018**, na.

(37) Zhang, S.; Park, Y.-S.; Li, J.; Lu, X.; Zhang, W.; Zhang, X. Negative Refractive Index in Chiral Metamaterials. *Phys. Rev. Lett.* **2009**, *102* (2), 023901.

(38) Rodrigues, S. P.; Lan, S.; Kang, L.; Cui, Y.; Cai, W. Nonlinear Imaging and Spectroscopy of Chiral Metamaterials. *Adv. Mater.* **2014**, *26* (35), 6157−6162.

(39) Valev, V. K.; Smisdom, N.; Silhanek, A. V.; De Clercq, B.; Gillijns, W.; Ameloot, M.; Moshchalkov, V. V.; Verbiest, T. Plasmonic Ratchet Wheels: Switching Circular Dichroism by Arranging Chiral Nanostructures. *Nano Lett.* **2009**, *9* (11), 3945−3948.

(40) Kawata, S.; Sun, H.-B.; Tanaka, T.; Takada, K. Finer Features for Functional Microdevices. *Nature* **2001**, *412* (6848), 697−698.

(41) Mark, A. G.; Gibbs, J. G.; Lee, T.-C.; Fischer, P. Hybrid Nanocolloids with Programmed Three-Dimensional Shape and Material Composition. *Nat. Mater.* **2013**, *12* (9), 802−807.

(42) Gibbs, J. G.; Mark, A. G.; Eslami, S.; Fischer, P. Plasmonic Nanohelix Metamaterials with Tailorable Giant Circular Dichroism. *Appl. Phys. Lett.* **2013**, *103* (21), 213101.

(43) Shen, X.; Song, C.; Wang, J.; Shi, D.; Wang, Z.; Liu, N.; Ding, B. Rolling Up Gold Nanoparticle-Dressed DNA Origami into Three-Dimensional Plasmonic Chiral Nanostructures. *J. Am. Chem. Soc.* **2012**, *134* (1), 146−149.

(44) Kuzyk, A.; Schreiber, R.; Fan, Z.; Pardatscher, G.; Roller, E.-M.; Högele, A.; Simmel, F. C.; Govorov, A. O.; Liedl, T. DNA-Based Self-Assembly of Chiral Plasmonic Nanostructures with Tailored Optical Response. *Nature* **2012**, *483* (7389), 311−314.

(45) Eftekhari, F.; Davis, T. J. Strong Chiral Optical Response from Planar Arrays of Subwavelength Metallic Structures Supporting Surface Plasmon Resonances. *Phys. Rev. B: Condens. Matter Mater. Phys.* **2012**, *86* (7), 075428.

(46) Liu, M.; Powell, D. A.; Shadrivov, I. V.; Lapine, M.; Kivshar, Y. S. Spontaneous Chiral Symmetry Breaking in Metamaterials. *Nat. Commun.* **2014**, *5*, 4441.

(47) Schwanecke, A. S.; Fedotov, V. A.; Khardikov, V. V.; Prosvirnin, S. L.; Chen, Y.; Zheludev, N. I. Nanostructured Metal Film with Asymmetric Optical Transmission. *Nano Lett.* **2008**, *8* (9), 2940−2943.

(48) Drezet, A.; Genet, C.; Laluet, J.-Y.; Ebbesen, T. W. Optical Chirality without Optical Activity: How Surface Plasmons Give a Twist to Light. *Opt. Express* **2008**, *16* (17), 12559−12570.

(49) Singh, R.; Plum, E.; Zhang, W.; Zheludev, N. I. Highly Tunable Optical Activity in Planar Achiral Terahertz Metamaterials. *Opt. Express* **2010**, *18* (13), 13425−13430.

(50) Xu, H.-X.; Wang, G.-M.; Qi, M. Q.; Cai, T.; Cui, T. J. Compact Dual-Band Circular Polarizer Using Twisted Hilbert-Shaped Chiral Metamaterial. *Opt. Express* **2013**, *21* (21), 24912−24921.

(51) Albooyeh, M.; Asadchy, V.; Zeng, J.; Kazemi, H.; Capolino, F. Applications and Potentials of Reciprocal Bianisotropic Metasurfaces. *arXiv:1811.04176 [physics.optics]* **2018**, na.

(52) Cai, W.; Chettiar, U. K.; Yuan, H.-K.; de Silva, V. C.; Kildishev, A. V.; Drachev, V. P.; Shalaev, V. M. Metamagnetics with Rainbow Colors. *Opt. Express* **2007**, *15* (6), 3333−3341.

(53) Graf, F.; Rockstuhl, C.; Fernandez-Corbaton, I. Helicity Preserving and Resonant Structures for Enhanced Chiral Molecule Detection. *ArXiv:181008385 Phys.* **2018**, na.

(54) Johnson, P. B.; Christy, R. W. Optical Constants of the Noble Metals. *Phys. Rev. B* **1972**, *6* (12), 4370−4379.

(55) Malitson, I. H. Interspecimen Comparison of the Refractive Index of Fused Silica*,†. *J. Opt. Soc. Am.* **1965**, *55* (10), 1205−1209.